ACS APPLIED MATERIALS & INTERFACES

www.acsami.org

Research Article

Giant Spin Hall Effect in Cu–Tb Alloy Thin Films

Zhan Xu, Grayson Dao Hwee Wong, Jiaxuan Tang, Er Liu, Weiliang Gan, Feng Xu,* and Wen Siang Lew*

Cite This: *ACS Appl. Mater. Interfaces* 2020, 12, 32898–32904

Read Online

ACCESS | Metrics & More | Article Recommendations | Supporting Information

ABSTRACT: We report the giant spin current generation in CuTb alloys arising from the spin Hall effect. The maximum spin Hall angle from our CuTb-based magnetic heterostructures was found to be −0.35 ± 0.02 for $Cu_{0.39}Tb_{0.61}$. We find that the contribution of skew scattering is larger than the side jump for lower Tb concentrations (<14.9%), while the converse is true for higher Tb concentrations. Additionally, we also studied the Gilbert damping parameter, spin diffusion length, and spin-mixing conductance. Interfacial spin transparency was found to be 0.55 ± 0.03 for the CoFeB/$Cu_{0.53}Tb_{0.47}$ interface. The spin diffusion length and spin-mixing conductance of the $Cu_{0.53}Tb_{0.47}$ alloy are λ_{sd} = 2.5 ± 0.3 nm and $G^{\uparrow\downarrow}$ = (24.2 ± 1.0) × 10^{15} cm^{-2}, respectively. Our results pave a way for rare-earth metals to be used as a spin Hall material in highly efficient SOT devices.

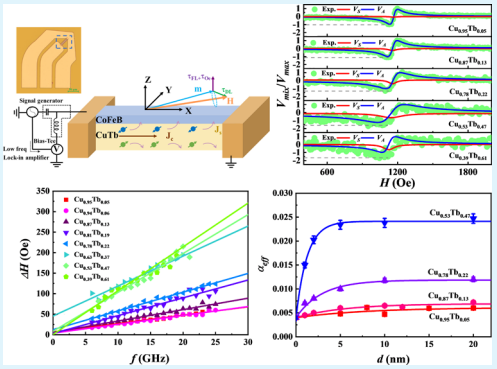

KEYWORDS: *spin Hall effect, spin–orbit coupling, spin–orbit torque, spin–orbit torque ferromagnetic resonance, rare-earth metal, spin Hall angle*

1. INTRODUCTION

Spintronic devices such as spin–orbit torque magnetic random access memories and spin Hall nano-oscillators are key components of next-generation magnetic storage and logic devices because of their high response speed and low power consumption.[1−5] Among them, the spin Hall effect (SHE) derived from the spin–orbit coupling (SOC) is a topic of immense interest because it can generate a longitudinal spin current when applying a lateral charge current, which is an efficient route for magnetization manipulation.[6−10] The spin Hall angle represents the conversion efficiency of the charge and spin current. A large spin Hall angle enables efficient generation of the transfer torque and reduces the energy loss. Moreover, the SHE plays an important role in exciting or detecting the spin Seebeck effect.[11−13] The large spin Hall angle can also lead to a high spin Seebeck coefficient in the magnon-driven spin Seebeck effect.[14−16] Therefore, the search for large spin Hall angles has long been a key focus in the field of spintronics.[17−20] To date, most studies have focused on heavy metals (HMs) such as Pt,[21−23] β-Ta,[4] and β-W;[24] diluted alloys of CuBi,[25] CuPt,[15,26] AuW,[27] WHf,[28] PtW,[16] AuPt,[17] and PtBi;[18] topological insulators;[29−31] and even antiferromagnetic materials.[32,33] The future development of high-performance devices hinges on the discovery of new types of large spin Hall angle materials.

Rare-earth metals have recently received considerable attention because of their large SOC that arises from their large spins and orbital angular momentum in f-electron atoms and are expected to be a potential SOT source for spintronic applications.[34−36] Several recent studies have reported that the spin Hall efficiency can be enhanced using rare-earth metals: Wong et al. have determined a large spin–orbit torque efficiency of −0.480 in Pt/$[Co/Ni]_2$/Co/Tb multilayers.[36] Ueda et al. conducted a study on Pt/Co/Gd multilayers and explained that the large spin Hall efficiency stemmed from Gd.[35] However, because of the strong spin-pumping effect caused by the strong SOC in heavy rare-earth materials, it is difficult to extract the spin Hall angle by using spin–torque ferromagnetic resonance. Reynolds et al. reported the lower bounds for the spin Hall torque ratio for Gd, Dy, Ho, and Lu by using a thin Hf spacer layer between the rare-earth and the FM to reduce the magnetic damping.[34] Therefore, it would be particularly useful to be able to control not only the spin Hall angle but also the magnetic damping.

In this work, we studied the giant spin Hall angle and moderately low effective magnetic damping in CoFeB/$Cu_{1-x}Tb_x$ bilayers. This material system was chosen for several reasons. First of all, Cu-based alloys have been widely reported for studying the effect of alloying on SHE.[15,19,25,26] Second, the Cu–Tb alloy can form a solid solution across a wide composition range from the phase diagram,[37] making it a

Received: April 22, 2020
Accepted: July 1, 2020
Published: July 1, 2020

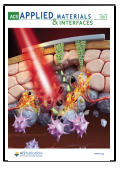

https://dx.doi.org/10.1021/acsami.0c07441
ACS Appl. Mater. Interfaces 2020, 12, 32898–32904

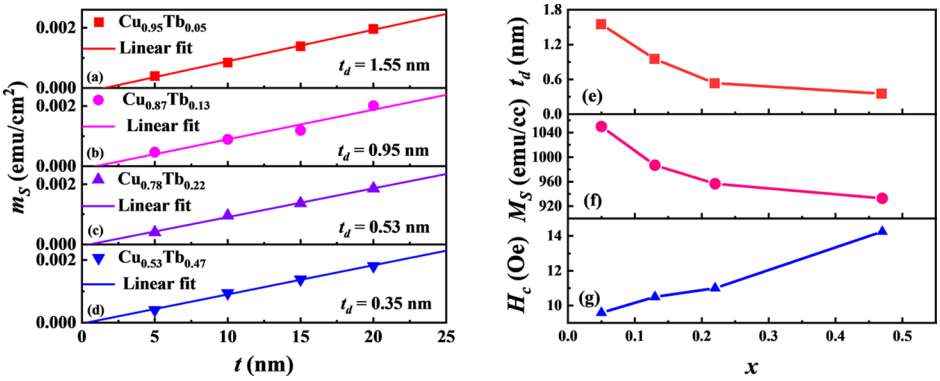

Figure 1. Measured moment per unit area of CoFeB/$Cu_{1-x}Tb_x$ films as a function of t for x = 0.05 (a), 0.13 (b), 0.22 (c), and 0.47 (d). Magnetic dead layer thickness (e), saturation magnetization M_S (f), and coercivity H_c (g) dependence on Tb concentration in CoFeB/$Cu_{1-x}Tb_x$ films.

suitable system to understand the mechanism of extrinsic SHE. Furthermore, an amorphous Cu−Tb alloy thin film has been reported by McGuire and Gambino,[38] which can be beneficial for pinning-free skyrmion dynamics because of the absence of grains.[28,39] By conducting spin−orbit torque ferromagnetic resonance (ST-FMR) measurements, we show that the maximum spin Hall angle of our CuTb-based magnetic heterostructures was −0.35 ± 0.02 for $Cu_{0.39}Tb_{0.61}$. From the extrinsic spin Hall resistivity induced by Tb, we found that the skew-scattering contribution dominates the extrinsic SHE at low Tb concentrations (x < 14.9%), whereas the side jump contribution is dominant when x > 14.9%. By varying the damping with CuTb thickness, we have determined the spin-mixing conductance and spin diffusion length. The effective spin-mixing conductance increases with increasing Tb concentration. Meanwhile, the spin diffusion length is found to increase with decreasing Tb concentrations. Furthermore, using the drift-diffusion model, we have estimated the interfacial spin transparency. These results provide important information on the large SHE induced by extrinsic SHE mechanisms, opening a way for rare-earth metals to be used as a spin Hall material in highly efficient SOT devices.

2. EXPERIMENT AND METHOD

Thin film stacks of $Co_{40}Fe_{40}B_{20}$ (20 nm)/$Cu_{1-x}Tb_x$ (10 nm) were deposited on thermally oxidized Si(001) substrates by magnetron sputtering. The growth was carried out at room temperature with a base pressure below 5×10^{-8} mTorr and a deposition pressure of 2 mTorr. $Cu_{1-x}Tb_x$ was deposited by cosputtering Cu and Tb targets. The sputtering power of the two targets was calibrated to tune the Tb concentration (x) in the $Cu_{1-x}Tb_x$ alloy. Subsequently, the stacks were patterned into strips (of length 50 μm and width 10 μm) using a combination of electron beam lithography and Ar-ion milling techniques. Ta (5 nm)/Cu (200 nm)/Pt (3 nm) electrodes were also fabricated using electron beam lithography and DC magnetron sputtering. The crystalline structure was examined by X-ray diffraction (XRD) and was found to be amorphous (refer to the Supporting Information, S1 XRD). The saturation magnetization was evaluated by using the vibrating sample magnetometer. The composition of alloy films was determined by energy-dispersive X-ray spectroscopy (EDX). A signal generator (Keysight N5183B) and a network analyzer were used to provide the radio frequency (RF) current for the ST-FMR and conventional FMR measurements, respectively. For ST-FMR studies, the DC voltage was measured with a Keithley 2000 multimeter. All the measurements were performed at room temperature.

3. RESULTS AND DISCUSSION

Figure 1a−d shows the CoFeB thickness t dependence of the magnetic moment per unit area at saturation m_S for x = 0.05, 0.13, 0.22, and 0.47, respectively. As the m_S is expressed as $M_S(t - t_d)$, where M_S is the saturation magnetization and t_d is the magnetic dead layer thickness in CoFeB, we evaluate M_S from the slope and t_d from the horizontal intercept by fitting with a linear function.[40] The effective saturation magnetization of CoFeB in the CoFeB/$Cu_{0.95}Tb_{0.05}$ system is found to be M_S = 1049.8 emu/cc with a magnetic dead layer t_d = 1.55 nm. The thickness of the dead layer t_d, saturation magnetization M_S, and coercivity H_c are summarized in Figure 1e−g. As the concentration of Tb increases, H_c increases, while both M_S and t_d decrease. The thickness of the magnetic dead layer and saturation magnetization were found to be 0.35 nm and 932.9 emu/cc, respectively, for $Cu_{0.53}Tb_{0.47}$. The reduction in the M_S value can be potentially due to compensation from the FM properties of Tb as the Tb atoms near the adjacent CoFeB atoms induces a non-zero magnetic moment. At the interface, the magnetic moments of Tb align antiparallel with the magnetic moments of CoFeB, leading to an antiferromagnetic coupling between the FM layer and Tb.[36,41,42] Additionally, the antiferromagnetic coupling gives rise to enhanced H_c. The magnetic dead layer could be due to the diffusion and intermixing at the CoFeB/$Cu_{1-x}Tb_x$ interface, which indicates a better interface in the Tb-rich alloy.

The schematic diagram of the ST-FMR measurement setup is illustrated in Figure 2. A RF current $I_{c,rf}$ is applied to the structure through the RF port of a bias tee to generate a microwave frequency SOT on the ferromagnetic layers, which induces magnetization precession. This leads to an oscillation of the longitudinal resistance due to the spin Hall magneto-resistance effect.[22] The rectified voltage V_{mix} due to the mixing of RF current and the time-varying resistance is detected by using a lock-in amplifier. The ST-FMR spectra were measured for microwave frequencies from 6 to 25 GHz for all samples without an external DC bias. An in-plane magnetic field was applied at an angle of 45° to maximize the ST-FMR signal and swept from 0 to 5000 Oe while keeping the microwave frequency constant for each measured frequency. The input microwave power was varied from 10 to 20 dBm, and the measured DC voltage was proportional to the applied power, suggesting that the induced precession was in the small angle

https://dx.doi.org/10.1021/acsami.0c07441
ACS Appl. Mater. Interfaces 2020, 12, 32898−32904

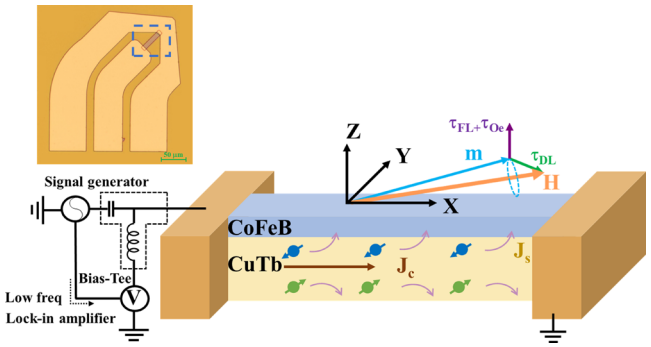

Figure 2. Schematic circuit for the ST-FMR measurement. M and H are the FM magnetization and applied magnetic field vectors, respectively. The $\tau_{FL} + \tau_{Oe}$ term denotes the sum of the field-like torque and the Oersted field torque, while τ_{DL} is the damping-like torque. J_C and J_S are the charge current density and the spin current density, respectively. Top left shows the optical image of the device with contact pads.

regime[23,43] (refer to the Supporting Information, S3 Input RF power dependence). All measurements were performed at an RF power of 18 dBm.

Figure 3a–e illustrates the normalized voltages (V_{mix}) measured at 13 GHz for x = 0.05, 0.13, 0.22, 0.47, and 0.61. The data were normalized to the maximum value of V_{mix}. The gray dashed line indicates the corresponding maximum of V_{mix}. The symmetric and antisymmetric Lorentzian components are presented in Figure 3a–e as the red and blue curves, respectively. The ST-FMR curves are fitted with symmetric and antisymmetric Lorentzian functions, according to[23,26,33]

$$V_{mix} = V_S \frac{(\Delta H)^2}{(\Delta H)^2 + (H - H_{res})^2} + V_A \frac{\Delta H(H - H_{res})}{(\Delta H)^2 + (H - H_{res})^2} \quad (1)$$

where ΔH is the full width at half-maximum and H_{res} is the resonance magnetic field. The symmetric and antisymmetric parameters V_S and V_A are the amplitudes of the symmetric and antisymmetric components of the mixing voltage, respectively. Here, the symmetric component is proportional to the damping-like torque, and the antisymmetric component is due to the sum of the Oersted field torque and the field-like effective torque.[23,44] The damping-like torque and the field-like torque can be expressed as $\mathbf{m} \times (\hat{\boldsymbol{\sigma}} \times \mathbf{m})$ and $\mathbf{m} \times \hat{\boldsymbol{\sigma}}$, respectively, where $\mathbf{m}$ is the magnetization unit vector and $\hat{\boldsymbol{\sigma}}$ denotes the direction of the injected spin moment.[22] The damping-like torque is generated by the spin current converted from the charge current flowing in the HM layer because of the SHE. As shown in Figure 3f, with increasing concentration of Tb, the magnitude of V_S/V_A increases, which suggests that the spin Hall angle increases with Tb concentration.

According to the ST-FMR theory, the spin Hall angle (θ_{SH}) is the ratio of the spin current density to the RF current density. The ratio can be obtained from the line shape of the ST-FMR spectra for a qualitative dependence of the θ_{SH} by assuming that the field-like torque contribution is negligibly small.[23,33] For the self-calibrated method, the θ_{SH} is given by

$$\theta_{SH} = \frac{eJ_S}{J_C} = \frac{V_S}{V_A} \frac{e\mu_0 M_S t d}{\hbar} \left(1 + \frac{4\pi M_{eff}}{H_{res}}\right)^{1/2} \quad (2)$$

where J_S is the spin current density generated within the HM, J_C is the applied charge current density, t is the FM layer thickness, d is the HM layer thickness, and M_{eff} is the effective magnetization, which can be extracted by fitting the resonance frequency f_{res} as a function of H_{res} using the Kittel formula, $f_{res} = (\gamma/2\pi)[H_{res}(H_{res} + 4\pi M_{eff})]^{1/2}$.

The calculated θ_{SH} are shown in Figure 4a. θ_{SH} was found to increase with increasing Tb concentration. This is expected, as the SHE arises from SOC and Tb is known to have a much larger SOC compared to Cu.[26] Furthermore, we observed that $Cu_{1-x}Tb_x$ with 61% Tb can give rise to θ_{SH} of -0.35 ± 0.02, which is larger than the reported value of -0.30 found in β-W.[24] With a further increase in the Tb concentration, the voltage signals become weak, leading to large noise of the spin Hall angle.

To determine the contribution of the extrinsic SHA due to Tb impurities, the extrinsic spin Hall resistivity induced by Tb was calculated and fitted using eq 3.[26] As the intrinsic SHE originates from the effect of SOC on the electronic band structure of hosts when in the dilute regime according to previous reports,[45–47] it can be assumed that the intrinsic spin Hall resistivity of CuTb is constant at low Tb concentrations. The electrical resistivity ρ of the $Cu_{1-x}Tb_x$ layer increases with increasing Tb concentration, as shown in the inset of Figure 4b. The $|\rho_{SH}^{imp}|$ was calculated from

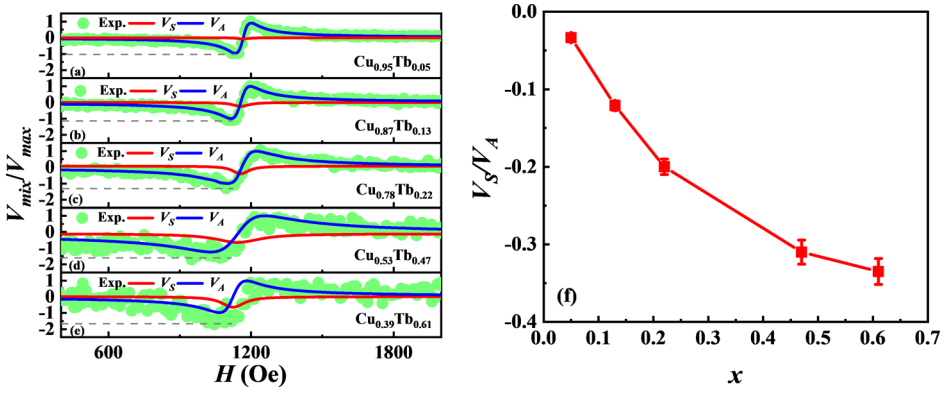

Figure 3. Normalized ST-FMR spectra of CoFeB/$Cu_{1-x}Tb_x$ with x = 0.05 (a), 0.13 (b), 0.22 (c), 0.47 (d), and 0.61 (e). (f) V_S/V_A as a function of x.

https://dx.doi.org/10.1021/acsami.0c07441
ACS Appl. Mater. Interfaces 2020, 12, 32898–32904

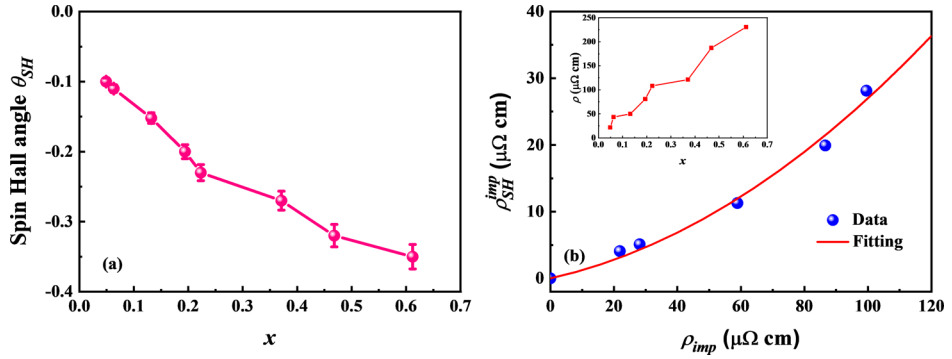

Figure 4. (a) θ_{SH} for different Tb concentrations extracted from ST-FMR spectra. (b) $|\rho_{SH}^{imp}|$ as a function of resistivity induced by Tb impurities. The inset shows the electrical resistivity of $Cu_{1-x}Tb_x$.

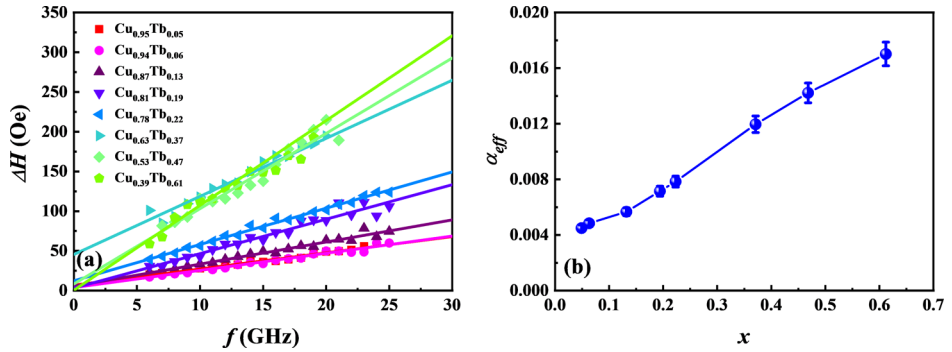

Figure 5. (a) FMR linewidths as a function of microwave frequency for different Tb concentrations. Solid lines were obtained by linear fits to the data points. (b) Effective Gilbert damping factor (α_{eff}) extracted from the ST-FMR linewidth as a function of different Tb concentrations.

$$|-\rho_{SH}^{imp}| = |\rho_{CuTb}\theta_{SH} - (\theta_{SH,Cu}/\rho_{Cu})\rho_{CuTb}^{2}| = \theta_{SH}^{SS}\rho_{imp} + \sigma_{SH}^{SJ}\rho_{imp}^{2} \quad (3)$$

where $\theta_{SH,Cu}$ is the spin Hall angle of pure Cu, $\rho_{imp} = \rho_{CuTb} - \rho_{Cu}$ is the resistance induced by Tb impurities, θ_{SH}^{SS} is the contributions of the skew scattering, and σ_{SH}^{SJ} is the contributions of the side jump.

The extrinsic spin Hall resistivity as a function of ρ_{imp} is shown in Figure 4b. From the fitting, we extract the following values: $\theta_{SH}^{SS} = 0.1059$ and $\sigma_{SH}^{SJ} = 0.0016\ \mu\Omega^{-1}\ cm^{-1}$. When $\rho_{imp} = \theta_{SH}^{SS}/\sigma_{SH}^{SJ} = 66.2\ \mu\Omega$ cm, which corresponds to $x \approx 14.9\%$, both the skew scattering and side jump contribution are equal. Therefore, skew scattering is dominant in the dilute limit of impurity concentration ($x < 14.9\%$), while the side jump contributions play a significant role at high impurity concentrations ($x > 14.9\%$), which agrees well with the previous reports.[26,45−47]

From the full width at half-maximum ΔH of ST-FMR spectra, the information about the damping factor (α_{eff}) can be obtained. The FMR linewidth of thin films has three main contributions: (1) an inhomogeneity term (ΔH_{inh}) which is independent of the frequency, (2) Gilbert damping term (ΔH_{Gil}) which is intrinsic in nature and frequency-dependent, and (3) a two-magnon scattering term (ΔH_{2mag}) which is extrinsic in nature and frequency-dependent.[48,49] The overall linewidth can be written as[50]

$$\Delta H = \Delta H_{inh} + \Delta H_{Gil} + \Delta H_{2mag} \quad (4)$$

Starting from the FMR linewidth, α_{eff} can be obtained from a linear fit of ΔH[50,51]

$$\Delta H(f) = \Delta H_{inh} + \frac{4\pi\alpha f}{|\gamma|\mu_0} \quad (5)$$

where $\gamma = (g\mu_B)/\hbar$ is the gyromagnetic ratio, g is the spectroscopic splitting factor, μ_B is the Bohr magneton, $\hbar$ is the reduced Planck's constant, and μ_0 is the permeability of free space. The frequency dependence of ΔH is summarized in Figure 5a. As Tb concentration increases, significant enhancement was observed in the slope of ΔH. The frequency dependence of ΔH for all the samples is linear, suggesting a negligible contribution from the two magnon-scattering mechanisms that would induce a nonlinear trend.[49]

The damping parameter was calculated using eq 5 for different Tb alloy concentrations, as shown in Figure 5b. The α_{eff} values are in the range from 0.0045 ± 0.0002 to 0.0170 ± 0.0008, which are lower than previous reports.[41,42] Increasing the Tb concentration leads to significant enhancement of the Gilbert damping parameter, which can be attributed to spin pumping. A spin current is generated from the ferromagnetic layer and diffuses into the nonmagnetic metallic layer when the magnetization precesses. In this process, the ferromagnetic layer loses the spin angular momentum, which results in additional damping. In our study, the damping contribution from the magnetic proximity effect is assumed to be negligibly small as the interfacial effect would be minimal in our relatively thick ferromagnetic layer.[51−54]

To determine the spin diffusion length (λ_{sd}) and the spin-mixing conductance ($G^{\uparrow\downarrow}$), a series of samples were fabricated with a fixed CoFeB thickness of 20 nm and a varied $Cu_{1-x}Tb_x$ thickness d. According to the spin pumping theory, the dependence of the damping on adjacent HM layer thickness can be described by[51,55]

https://dx.doi.org/10.1021/acsami.0c07441
ACS Appl. Mater. Interfaces 2020, 12, 32898−32904

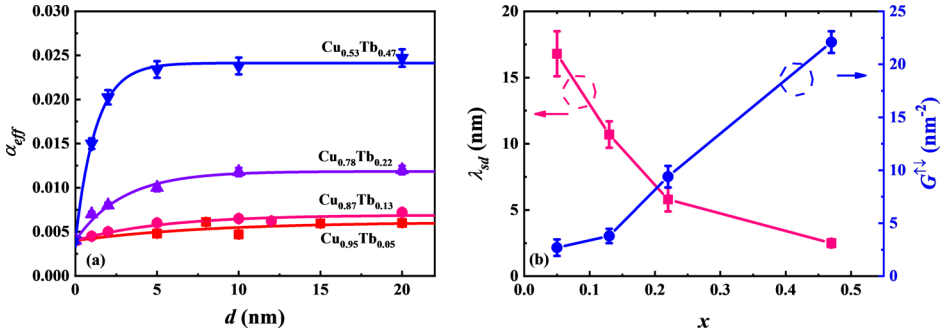

Figure 6. (a) Gilbert damping in CoFeB/$Cu_{1-x}Tb_x$ as a function of $Cu_{1-x}Tb_x$ thickness for x = 0.05, 0.13, 0.22, and 0.47. Solid lines are theoretical fit by the spin-pumping theory. (b) Spin diffusion length (λ_{sd}) and spin-mixing conductance ($G^{\uparrow\downarrow}$) dependence on Tb concentration in CoFeB/$Cu_{1-x}Tb_x$ films.

$$\alpha_{eff} = \alpha_{FM} + \frac{g\mu_B}{4\pi M_s(t - t_d)} G^{\downarrow\uparrow}(1 - e^{-2d/\lambda_{sd}}) \quad (6)$$

Figure 6a summarizes the damping due to spin pumping with varying thickness. The solid lines are fits for each composition. Damping was found to increase sharply in the lower thickness regime before saturating at a higher thickness. However, this exponential behavior for the enhanced damping as a function of d is inconsistent with the magnetic proximity effect-induced additional damping, which is a quasilinear thickness dependence of damping.[53,54] This indicates that there is no evidence that the magnetic proximity effect affects α_{eff}. The spin diffusion length deteriorates with increasing Tb concentration because of the strong SOC in Tb impurities that result in spin relaxation.

From the fit for thickness dependence of each Tb concentration, we calculated the diffusion length λ_{sd}, as plotted in Figure 6b. The obtained λ_{sd} decreases from 16.8 ± 1.7 nm for $Cu_{0.95}Tb_{0.05}$ to 2.5 ± 0.3 nm for $Cu_{0.53}Tb_{0.47}$ with the increase of Tb concentration. The spin diffusion length of $Cu_{0.53}Tb_{0.47}$ is comparable to that of Pt (λ_{sd} = 2.8 nm).[53] However, it is much smaller than what was reported by Yue et al.,[41] which may be due to the strong scattering caused by Tb impurities in our system, and this is consistent with other reports on HM alloys such as CuIr[56] and $Au_{1-x}Pt_x$.[45] The spin-mixing conductance for the CoFeB/$Cu_{0.53}Tb_{0.47}$ interface is (24.2 ± 1.0) × 10^{15} cm^{-2}, which is of the same order of magnitude as the Py/Tb ($G^{\uparrow\downarrow}_{Py/Tb}$ = 68 × 10^{15} cm^{-2}) interface.[41] It is to be noted that the voltage signal from the spin-pumping effect (V_{SP}) has a negligible effect on the symmetric component of the voltage signal because of a large anisotropic magnetoresistance (refer to the Supporting Information).[57] Furthermore, a large interface spin transparency (T) is required for low-energy consumption applications of spin current in multilayered devices.[58,59] The interface spin transparency can be estimated from the drift-diffusion model[57]

$$T = \frac{G^{\uparrow\downarrow}\tanh\left(\frac{d}{2\lambda_{sd}}\right)}{G^{\uparrow\downarrow}\coth\left(\frac{d}{\lambda_{sd}}\right) + \frac{h}{2\lambda e^2 \rho_{CuTb}}} \quad (7)$$

The interface spin transparency of CoFeB/$Cu_{0.53}Tb_{0.47}$ was estimated to be 0.55 ± 0.03, which is larger than that in CoFeB/β-Ta (0.50)[60] and comparable with the value of Co/Pt interfaces (0.3−0.67).[55]

4. CONCLUSIONS

In summary, we demonstrated the enhancement of the spin Hall angle by tuning the composition of CuTb alloy thin films. The giant spin Hall angle in the CuTb alloy is due to the strong spin−orbit interaction from the Tb impurities. We found that the contribution of skew scattering dominates side jump at lower Tb concentrations (<14.9%), while the side jump contributions play a significant role at higher Tb concentrations. We also obtained the spin diffusion length and spin-mixing conductance for the CuTb alloy. Furthermore, we extracted the interfacial spin transparency of CoFeB/$Cu_{0.53}Tb_{0.47}$ as 0.55 ± 0.03, which is comparable with various studied HM/FM interfaces. The giant θ_{SH} and high effective spin-mixing conductance with moderate interfacial spin transparency of CoFeB/$Cu_{1-x}Tb_x$ make it a key spin Hall material in highly efficient SOT devices.

■ ASSOCIATED CONTENT

Supporting Information

The Supporting Information is available free of charge at https://pubs.acs.org/doi/10.1021/acsami.0c07441.

XRD patterns; M−H loops; input RF power dependence; inhomogeneous linewidth broadening; spurious voltage signal due to spin pumping; and influence of interfacial antiferromagnetic coupling (PDF)

■ AUTHOR INFORMATION

Corresponding Authors

Feng Xu − *MIIT Key Laboratory of Advanced Metallic and Intermetallic Materials Technology, School of Materials Science and Engineering, Nanjing University of Science and Technology, Nanjing 210094, China;* orcid.org/0000-0001-5802-7925; Email: xufeng@njust.edu.cn

Wen Siang Lew − *School of Physical and Mathematical Sciences, Nanyang Technological University, Singapore 637371 Singapore;* orcid.org/0000-0002-5161-741X; Email: wensiang@ntu.edu.sg

Authors

Zhan Xu − *School of Physical and Mathematical Sciences, Nanyang Technological University, Singapore 637371 Singapore; MIIT Key Laboratory of Advanced Metallic and Intermetallic Materials Technology, School of Materials Science and Engineering, Nanjing University of Science and Technology, Nanjing 210094, China;* orcid.org/0000-0003-1224-9789

https://dx.doi.org/10.1021/acsami.0c07441
ACS Appl. Mater. Interfaces 2020, 12, 32898−32904

Grayson Dao Hwee Wong − *School of Physical and Mathematical Sciences, Nanyang Technological University, Singapore 637371 Singapore*

Jiaxuan Tang − *MIIT Key Laboratory of Advanced Metallic and Intermetallic Materials Technology, School of Materials Science and Engineering, Nanjing University of Science and Technology, Nanjing 210094, China*

Er Liu − *MIIT Key Laboratory of Advanced Metallic and Intermetallic Materials Technology, School of Materials Science and Engineering, Nanjing University of Science and Technology, Nanjing 210094, China;* orcid.org/0000-0001-9534-7469

Weiliang Gan − *School of Physical and Mathematical Sciences, Nanyang Technological University, Singapore 637371 Singapore*

Complete contact information is available at: https://pubs.acs.org/10.1021/acsami.0c07441

Author Contributions

Z.X. conceived the idea and designed this work. G.D.H.W. and J.T. assisted in the development of the experimental setup. E.L. and W.L.G. made scientific comments on the results. W.S.L. and F.X. coordinated and supervised the entire work. All authors contributed to the discussion and manuscript writing.

Notes

The authors declare no competing financial interest.

■ ACKNOWLEDGMENTS

This work was supported by the RIE2020 AME-IAF-ICP grant (no. I1801E0030). This work was also supported by an EDB-IPP (RCA—17/284) program and an Industry-IHL Partnership Program (NRF2015-IIP001-001). Z.X. gratefully acknowledges financial support from the China Scholarship Council.

■ REFERENCES

(1) Avci, C. O.; Quindeau, A.; Pai, C.-F.; Mann, M.; Caretta, L.; Tang, A. S.; Onbasli, M. C.; Ross, C. A.; Beach, G. S. D. Current-Induced Switching in a Magnetic Insulator. *Nat. Mater.* **2017**, *16*, 309−314.

(2) Miron, I. M.; Garello, K.; Gaudin, G.; Zermatten, P.-J.; Costache, M. V.; Auffret, S.; Bandiera, S.; Rodmacq, B.; Schuhl, A.; Gambardella, P. Perpendicular Switching of a Single Ferromagnetic Layer Induced by In-Plane Current Injection. *Nature* **2011**, *476*, 189−193.

(3) Emori, S.; Bauer, U.; Ahn, S.-M.; Martinez, E.; Beach, G. S. D. Current-Driven Dynamics of Chiral Ferromagnetic Domain Walls. *Nat. Mater.* **2013**, *12*, 611−616.

(4) Liu, L.; Pai, C.-F.; Li, Y.; Tseng, H. W.; Ralph, D. C.; Buhrman, R. A. Spin-Torque Switching with the Giant Spin Hall Effect of Tantalum. *Science* **2012**, *336*, 555−558.

(5) Haazen, P. P. J.; Murè, E.; Franken, J. H.; Lavrijsen, R.; Swagten, H. J. M.; Koopmans, B. Domain Wall Depinning Governed by the Spin Hall Effect. *Nat. Mater.* **2013**, *12*, 299−303.

(6) Sinova, J.; Valenzuela, S. O.; Wunderlich, J.; Back, C. H.; Jungwirth, T. Spin Hall Effects. *Rev. Mod. Phys.* **2015**, *87*, 1213−1260.

(7) Soumyanarayanan, A.; Reyren, N.; Fert, A.; Panagopoulos, C. Emergent Phenomena Induced by Spin-Orbit Coupling at Surfaces and Interfaces. *Nature* **2016**, *539*, 509−517.

(8) Luo, F.; Wong, Q. Y.; Li, S.; Tan, F.; Lim, G. J.; Wang, X.; Lew, W. S. Dependence of Spin-Orbit Torque Effective Fields on Magnetization Uniformity in Ta/Co/Pt Structure. *Sci. Rep.* **2019**, *9*, 1−7.

(9) Ramu, M.; Goolaup, S.; Gan, W. L.; Krishnia, S.; Lim, G. J.; Lew, W. S. Spin Orbit Torque Induced Asymmetric Depinning of Chiral Néel Domain Wall in Co/Ni Heterostructures. *Appl. Phys. Lett.* **2017**, *110*, 162402.

(10) Li, S.; Goolaup, S.; Kwon, J.; Luo, F.; Gan, W.; Lew, W. S. Deterministic Spin-Orbit Torque Induced Magnetization Reversal in Pt/[Co/Ni]n/Co/Ta Multilayer Hall Bars. *Sci. Rep.* **2017**, *7*, 1−9.

(11) Vlietstra, N.; Shan, J.; Van Wees, B. J.; Isasa, M.; Casanova, F.; Ben Youssef, J. Simultaneous Detection of the Spin-Hall Magnetoresistance and the Spin-Seebeck Effect in Platinum and Tantalum on Yttrium Iron Garnet. *Phys. Rev. B: Condens. Matter Mater. Phys.* **2014**, *90*, 174436.

(12) Kattel, S.; Murphy, J. R.; Ellsworth, D.; Ding, J.; Liu, T.; Li, P.; Wu, M.; Rice, W. D. Broadband Optical Detection Using the Spin Seebeck Effect. *Phys. Rev. Appl.* **2019**, *12*, 034047.

(13) Seifert, T. S.; Jaiswal, S.; Barker, J.; Weber, S. T.; Razdolski, I.; Cramer, J.; Gueckstock, O.; Maehrlein, S. F.; Nadvornik, L.; Watanabe, S.; Ciccarelli, C.; Melnikov, A.; Jakob, G.; Münzenberg, M.; Goennenwein, S. T. B.; Woltersdorf, G.; Rethfeld, B.; Brouwer, P. W.; Wolf, M.; Kläui, M.; Kampfrath, T. Femtosecond Formation Dynamics of the Spin Seebeck Effect Revealed by Terahertz Spectroscopy. *Nat. Commun.* **2018**, *9*, 1−11.

(14) Xiao, J.; Bauer, G. E. W.; Uchida, K. C.; Saitoh, E.; Maekawa, S. Theory of Magnon-Driven Spin Seebeck Effect. *Phys. Rev. B: Condens. Matter Mater. Phys.* **2010**, *81*, 214418.

(15) Tian, K.; Tiwari, A. CuPt Alloy Thin Films for Application in Spin Thermoelectrics. *Sci. Rep.* **2019**, *9*, 1−6.

(16) Uchida, K.-i.; Sasaki, M.; Sakuraba, Y.; Iguchi, R.; Daimon, S.; Saitoh, E.; Goto, M. Combinatorial Investigation of Spin-Orbit Materials Using Spin Peltier Effect. *Sci. Rep.* **2018**, *8*, 1−7.

(17) Zhu, L.; Ralph, D. C.; Buhrman, R. A. Highly Efficient Spin-Current Generation by the Spin Hall Effect in Au 1 − x Pt X. *Phys. Rev. Appl.* **2018**, *10*, 031001.

(18) Hong, C.; Jin, L.; Zhang, H.; Li, M.; Rao, Y.; Ma, B.; Li, J.; Zhong, Z.; Yang, Q. Giant Inverse Spin Hall Effect in Bi Doped PtBi Alloy. *Adv. Electron. Mater.* **2018**, *4*, 1700632.

(19) Musha, A.; Kanno, Y.; Ando, K. Extrinsic-Intrinsic Crossover of the Spin Hall Effect Induced by Alloying. *Phys. Rev. Mater.* **2019**, *3*, 054411.

(20) Derunova, E.; Sun, Y.; Felser, C.; Parkin, S. S. P.; Yan, B.; Ali, M. N. Giant Intrinsic Spin Hall Effect in W3Ta and Other A15 Superconductors. *Sci. Adv.* **2019**, *5*, No. eaav8575.

(21) Oh, Y.-W.; Chris Baek, S.-h.; Kim, Y. M.; Lee, H. Y.; Lee, K.-D.; Yang, C.-G.; Park, E.-S.; Lee, K.-S.; Kim, K.-W.; Go, G.; Jeong, J.-R.; Min, B.-C.; Lee, H.-W.; Lee, K.-J.; Park, B.-G. Field-Free Switching of Perpendicular Magnetization through Spin-Orbit Torque in Antiferromagnet/Ferromagnet/Oxide Structures. *Nat. Nanotechnol.* **2016**, *11*, 878−884.

(22) Liu, L.; Moriyama, T.; Ralph, D. C.; Buhrman, R. A. Spin-Torque Ferromagnetic Resonance Induced by the Spin Hall Effect. *Phys. Rev. Lett.* **2011**, *106*, 036601.

(23) Wang, Y.; Deorani, P.; Qiu, X.; Kwon, J. H.; Yang, H. Determination of Intrinsic Spin Hall Angle in Pt. *Appl. Phys. Lett.* **2014**, *105*, 152412.

(24) Pai, C. F.; Liu, L.; Li, Y.; Tseng, H. W.; Ralph, D. C.; Buhrman, R. A. Spin Transfer Torque Devices Utilizing the Giant Spin Hall Effect of Tungsten. *Appl. Phys. Lett.* **2012**, *101*, 122404.

(25) Niimi, Y.; Kawanishi, Y.; Wei, D. H.; Deranlot, C.; Yang, H. X.; Chshiev, M.; Valet, T.; Fert, A.; Otani, Y. Giant Spin Hall Effect Induced by Skew Scattering from Bismuth Impurities inside Thin Film CuBi Alloys. *Phys. Rev. Lett.* **2012**, *109*, 156602.

(26) Ramaswamy, R.; Wang, Y.; Elyasi, M.; Motapothula, M.; Venkatesan, T.; Qiu, X.; Yang, H. Extrinsic Spin Hall Effect in Cu1-XPtx. *Phys. Rev. Appl.* **2017**, *8*, 024034.

(27) Laczkowski, P.; Rojas-Sánchez, J.-C.; Savero-Torres, W.; Jaffrès, H.; Reyren, N.; Deranlot, C.; Notin, L.; Beigné, C.; Marty, A.; Attané, J.-P.; Vila, L.; George, J.-M.; Fert, A. Experimental Evidences of a Large Extrinsic Spin Hall Effect in AuW Alloy. *Appl. Phys. Lett.* **2014**, *104*, 142403.

(28) Fritz, K.; Wimmer, S.; Ebert, H.; Meinert, M. Large Spin Hall Effect in an Amorphous Binary Alloy. *Phys. Rev. B* **2018**, *98*, 094433.

(29) Wang, Y.; Deorani, P.; Banerjee, K.; Koirala, N.; Brahlek, M.; Oh, S.; Yang, H. Topological Surface States Originated Spin-Orbit Torques in Bi2Se3. *Phys. Rev. Lett.* **2015**, *114*, 257202.
(30) Wang, Y.; Zhu, D.; Wu, Y.; Yang, Y.; Yu, J.; Ramaswamy, R.; Mishra, R.; Shi, S.; Elyasi, M.; Teo, K. L.; Wu, Y.; Yang, H. Room Temperature Magnetization Switching in Topological Insulator-Ferromagnet Heterostructures by Spin-Orbit Torques. *Nat. Commun.* **2017**, *8*, 6−11.
(31) Mellnik, A. R.; Lee, J. S.; Richardella, A.; Grab, J. L.; Mintun, P. J.; Fischer, M. H.; Vaezi, A.; Manchon, A.; Kim, E.-A.; Samarth, N.; Ralph, D. C. Spin-Transfer Torque Generated by a Topological Insulator. *Nature* **2014**, *511*, 449−451.
(32) Zhang, W.; Han, W.; Yang, S.-H.; Sun, Y.; Zhang, Y.; Yan, B.; Parkin, S. S. P. Giant Facet-Dependent Spin-Orbit Torque and Spin Hall Conductivity in the Triangular Antiferromagnet IrMn 3. *Sci. Adv.* **2016**, *2*, No. e1600759.
(33) Zhou, J.; Wang, X.; Liu, Y.; Yu, J.; Fu, H.; Liu, L.; Chen, S.; Deng, J.; Lin, W.; Shu, X.; Yoong, H. Y.; Hong, T.; Matsuda, M.; Yang, P.; Adams, S.; Yan, B.; Han, X.; Chen, J. Large Spin-Orbit Torque Efficiency Enhanced by Magnetic Structure of Collinear Antiferromagnet IrMn. *Sci. Adv.* **2019**, *5*, No. eaau6696.
(34) Reynolds, N.; Jadaun, P.; Heron, J. T.; Jermain, C. L.; Gibbons, J.; Collette, R.; Buhrman, R. A.; Schlom, D. G.; Ralph, D. C. Spin Hall Torques Generated by Rare-Earth Thin Films. *Phys. Rev. B* **2017**, *95*, 1−12.
(35) Ueda, K.; Pai, C. F.; Tan, A. J.; Mann, M.; Beach, G. S. D. Effect of Rare Earth Metal on the Spin-Orbit Torque in Magnetic Heterostructures. *Appl. Phys. Lett.* **2016**, *108*, 232405.
(36) Wong, Q. Y.; Murapaka, C.; Law, W. C.; Gan, W. L.; Lim, G. J.; Lew, W. S. Enhanced Spin-Orbit Torques in Rare-Earth Pt/[Co/Ni] 2/Co/Tb Systems. *Phys. Rev. Appl.* **2019**, *11*, 024057.
(37) Predel, B. *Cu-Tb (Copper-Terbium): Datasheet from Landolt-Börnstein - Group IV Physical Chemistry ·Volume 5D: "Cr-Cs−Cu-Zr" in SpringerMaterials*; Springer-Verlag Berlin Heidelberg, 1994.
(38) McGuire, T. R.; Gambino, R. J. Magnetic and Transport Properties of Rare-Earth Au and Cu Amorphous Alloys. *J. Appl. Phys.* **1979**, *50*, 7653−7655.
(39) Legrand, W.; Maccariello, D.; Reyren, N.; Garcia, K.; Moutafis, C.; Moreau-Luchaire, C.; Collin, S.; Bouzehouane, K.; Cros, V.; Fert, A. Room-Temperature Current-Induced Generation and Motion of Sub-100 Nm Skyrmions. *Nano Lett.* **2017**, *17*, 2703−2712.
(40) Liu, T.; Zhang, Y.; Cai, J. W.; Pan, H. Y. Thermally Robust Mo/CoFeB/MgO Trilayers with Strong Perpendicular Magnetic Anisotropy. *Sci. Rep.* **2015**, *4*, 5895.
(41) Yue, J.; Jiang, S.; Zhang, D.; Yuan, H.; Wang, Y.; Lin, L.; Zhai, Y.; Du, J.; Zhai, H. The Influence of Interface on Spin Pumping Effect in Ni_{80} Fe_{20} /Tb Bilayer. *AIP Adv.* **2016**, *6*, 056120.
(42) Sun, L.; Yue, J.; Jiang, S.; Xu, Y.; Li, Q.; Chen, Q.; Zhou, X.; Huang, Z.; Yao, Z.; Zhai, Y.; Zhai, H. Influence of Cr Layer Thickness on the Static and Dynamic Performances of Tb/Cr/Ni80Fe20structure. *J. Alloys Compd.* **2017**, *695*, 1324−1328.
(43) Liu, T.; Li, Y.; Gu, L.; Ding, J.; Chang, H.; Janantha, P. A. P.; Kalinikos, B.; Novosad, V.; Hoffmann, A.; Wu, R.; Chien, C. L.; Wu, M. Nontrivial Nature and Penetration Depth of Topological Surface States in SmB6 Thin Films. *Phys. Rev. Lett.* **2018**, *120*, 207206.
(44) Kurebayashi, H.; Sinova, J.; Fang, D.; Irvine, A. C.; Skinner, T. D.; Wunderlich, J.; Novák, V.; Campion, R. P.; Gallagher, B. L.; Vehstedt, E. K.; Zârbo, L. P.; Výborný, K.; Ferguson, A. J.; Jungwirth, T. An Antidamping Spin-Orbit Torque Originating from the Berry Curvature. *Nat. Nanotechnol.* **2014**, *9*, 211−217.
(45) Isasa, M.; Villamor, E.; Hueso, L. E.; Gradhand, M. Temperature Dependence of Spin Diffusion Length and Spin Hall Angle in Au and Pt. *Phys. Rev. B* **2015**, *91*, 024402.
(46) Hou, D.; Su, G.; Tian, Y.; Jin, X.; Yang, S. A.; Niu, Q. Multivariable Scaling for the Anomalous Hall Effect. *Phys. Rev. Lett.* **2015**, *114*, 217203.
(47) Niimi, Y.; Otani, Y. Reciprocal Spin Hall Effects in Conductors with Strong Spin-Orbit Coupling: A Review. *Rep. Prog. Phys.* **2015**, *78*, 124501.
(48) Mills, D. L.; Arias, R. The Damping of Spin Motions in Ultrathin Films: Is the Landau-Lifschitz-Gilbert Phenomenology Applicable? *Phys. B* **2006**, *384*, 147−151.
(49) Zakeri, K.; Lindner, J.; Barsukov, I.; Meckenstock, R.; Farle, M.; Von Hörsten, U.; Wende, H.; Keune, W.; Rocker, J.; Kalarickal, S. S.; Lenz, K.; Kuch, W.; Baberschke, K.; Frait, Z. Spin Dynamics in Ferromagnets: Gilbert Damping and Two-Magnon Scattering. *Phys. Rev. B: Condens. Matter Mater. Phys.* **2007**, *76*, 1−8.
(50) Schoen, M. A. W.; Thonig, D.; Schneider, M. L.; Silva, T. J.; Nembach, H. T.; Eriksson, O.; Karis, O.; Shaw, J. M. Ultra-Low Magnetic Damping of a Metallic Ferromagnet. *Nat. Phys.* **2016**, *12*, 839−842.
(51) Shaw, J. M.; Nembach, H. T.; Silva, T. J. Determination of Spin Pumping as a Source of Linewidth in Sputtered Co 90Fe 10/Pd Multilayers by Use of Broadband Ferromagnetic Resonance Spectroscopy. *Phys. Rev. B: Condens. Matter Mater. Phys.* **2012**, *85*, 054412.
(52) Koyama, T.; Guan, Y.; Hibino, Y.; Suzuki, M.; Chiba, D. Magnetization Switching by Spin-Orbit Torque in Pt with Proximity-Induced Magnetic Moment. *J. Appl. Phys.* **2017**, *121*, 123903.
(53) Caminale, M.; Ghosh, A.; Auffret, S.; Ebels, U.; Ollefs, K.; Wilhelm, F.; Rogalev, A.; Bailey, W. E. Spin Pumping Damping and Magnetic Proximity Effect in Pd and Pt Spin-Sink Layers. *Phys. Rev. B* **2016**, *94*, 014414.
(54) Sun, Y.; Chang, H.; Kabatek, M.; Song, Y.-Y.; Wang, Z.; Jantz, M.; Schneider, W.; Wu, M.; Montoya, E.; Kardasz, B.; Heinrich, B.; te Velthuis, S. G. E.; Schultheiss, H.; Hoffmann, A. Damping in Yttrium Iron Garnet Nanoscale Films Capped by Platinum. *Phys. Rev. Lett.* **2013**, *111*, 106601.
(55) Pai, C. F.; Ou, Y.; Vilela-Leão, L. H.; Ralph, D. C.; Buhrman, R. A. Dependence of the Efficiency of Spin Hall Torque on the Transparency of Pt/Ferromagnetic Layer Interfaces. *Phys. Rev. B: Condens. Matter Mater. Phys.* **2015**, *92*, 064426.
(56) Belmeguenai, M.; Gabor, M. S.; Zighem, F.; Tiusan, C. Damping and Spin Mixing Conductance in Ni 80 Fe 20 /CuIr Structures: Effect of Ir Doping. *J. Phys. D: Appl. Phys.* **2017**, *50*, 135002.
(57) Zhang, W.; Han, W.; Jiang, X.; Yang, S.-H.; S. P. Parkin, S. Role of Transparency of Platinum-Ferromagnet Interfaces in Determining the Intrinsic Magnitude of the Spin Hall Effect. *Nat. Phys.* **2015**, *11*, 496−502.
(58) Zhu, L.; Ralph, D. C.; Buhrman, R. A. Enhancement of Spin Transparency by Interfacial Alloying. *Phys. Rev. B* **2019**, *99*, 180404.
(59) Zhu, L.; Ralph, D. C.; Buhrman, R. A. Spin-Orbit Torques in Heavy-Metal − Ferromagnet Bilayers with Varying Strengths of Interfacial Spin-Orbit Coupling. *Phys. Rev. Lett.* **2019**, *122*, 77201.
(60) Panda, S. N.; Mondal, S.; Sinha, J.; Choudhury, S.; Barman, A. All-Optical Detection of Interfacial Spin Transparency from Spin Pumping in b -Ta/CoFeB Thin Films. *Sci. Adv.* **2019**, *5*, No. eaav7200.

https://dx.doi.org/10.1021/acsami.0c07441
ACS Appl. Mater. Interfaces 2020, 12, 32898−32904